On the challenges of estimating the low-wavenumber wall pressure field beneath a turbulent boundary layer using a microphone array

Hesam Abtahi, Mahmoud Karimi, Laurent Maxit

On the Challenges of Estimating the Low-wavenumber Wall Pressure Field beneath a Turbulent Boundary Layer using a Microphone Array

Hesam Abtahi[a], Mahmoud Karimi[a], Laurent Maxit[b]

[a] *Centre for Audio, Acoustics and Vibration, University of Technology Sydney, Sydney, Australia*

[b] *Univ Lyon, INSA–Lyon, Laboratoire Vibrations-Acoustique (LVA), 25 bis, av. Jean Capelle, F-69621, Villeurbanne Cedex, France*

Abstract

The low-wavenumber components of the turbulent boundary layer (TBL) wall pressure field (WPF) are known to be the primary cause of structural vibration in low-Mach number flows, despite the maximal energy of the TBL being at the convective wavenumber. Existing semi-empirical TBL models show good agreement in predicting the WPF levels in convective region but differ significantly in the low-wavenumber domain. This study aims to highlight the challenges of estimating the low-wavenumber WPF in a TBL using a microphone array. A regularized Fourier-based approach is proposed to numerically study the estimation of the low-wavenumber WPF. Performance of the proposed method is initially evaluated by comparing the estimated WPF against a closed-form input TBL model. Effects of sensor spacing, co-array factor, and sensor distribution on the estimation of the low-wavenumber WPF levels are then investigated. To mimic experimental measurements, a virtual acoustic experiment is proposed, involving the synthesis of snapshots of TBL-induced WPF. It is demonstrated that although with relatively small number of snapshots the convective region can be identified, a significant number of snapshots is required to well estimate the TBL low-wavenumber region.

Email addresses: Seyedhesamaldin.Abtahi@student.uts.edu.au (Hesam Abtahi), Mahmoud.Karimi@uts.edu.au (Mahmoud Karimi), Laurent.Maxit@insa-lyon.fr (Laurent Maxit)

Keywords: turbulent boundary layer, wall pressure fluctuations, microphone array, low-wavenumber domain, virtual acoustic experiment

1. Introduction

The interaction of a fluid flow with structures generates vibration and noise, which has significant implications in many engineering applications, including the vibration and noise produced in water transport pipelines, the prediction and reduction of aircraft cabin noise, and sound generation in automobiles [1, 2, 3]. Different internal and external forces can cause the vibration and radiated noise of these structures. TBL, as one of the main noise and vibration contributors, generates pressure fluctuations over a surface, subsequently imposing an unsteady load on the structure that leads to noise and vibrations.

Although the maximum energy of the TBL occurs around the convective wavenumber, it is known that the low-wavenumber components of the WPF beneath a TBL is the main cause of structural vibration in low Mach number flows associated with marine applications [4, 5, 6, 7]. This is because the structure filters the convective ridge of the TBL excitation at frequencies well above the aerodynamic coincidence frequency [8]. This has been graphically illustrated in Fig. 1 where the schematic of spatial matching of the wavenumber-frequency spectrum of the TBL WPF, $\phi_{pp}(k,\omega)$, and vibration modal response of the structure, $\Psi_s(k,\omega)$, are plotted under the condition $U_c < c_b < c_0$ where U_c, c_b and c_0 are the fluid convective velocity, bending wave speed of the structure and speed of sound, respectively. The vibration response of the structure can be mathematically determined by integrating the product of the WPF excitation and modal response of the structures in the wavenumber domain [3]. Therefore, accurate estimation of the WPF in this region is of paramount importance to the prediction of TBL-induced vibrations.

A variety of semi-empirical TBL models have been developed and are available in literature such as the Corcos [9], Mellen [10] and chase [11]. Despite the fact that most models are in good agreement when it comes to predicting the convective region, there is a significant discrepancy at subconvective region as shown in Fig. 2. Historically, it has been difficult to model and measure the low-wavenumber levels of the TBL WPF due to their relatively low amplitudes compared to the amplitude of the WPF at convective wavenumber. Moreover, most of the existing body of research on

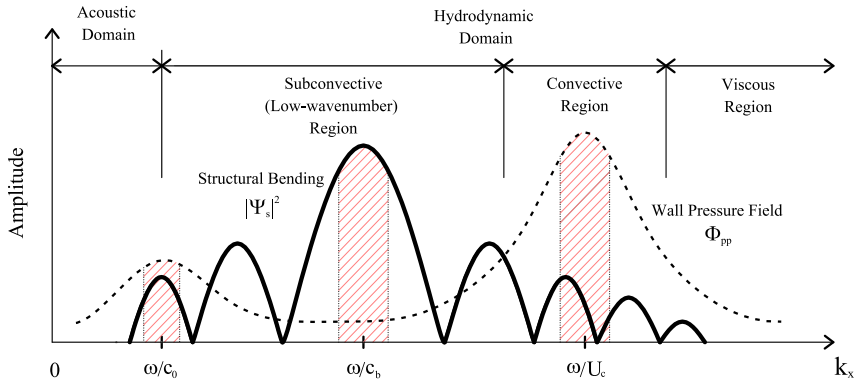

Fig. 1. Schematic of the spatial matching of the wavenumber-frequency spectrum of the TBL WPF and vibration modal function when $U_c < c_b < c_0$ (not in scale). The solid thick line represents the squared magnitude of the structural mode shape, while the dashed line represents the WPF.

estimation of the TBL WPF focuses on the convective ridge and not on the low-wavenumber region despite of its importance. This highlights the need for further study to better understand the process of identification of the low-wavenumber WPF. Hence, this work aims to investigate the key parameters in the estimation of the low-wavenumber WPF beneath a TBL using numerical study.

Microphone arrays are typically used to measure the WPF. They directly capture the sound waves generated by the WPF. To estimate the WPF, microphones are usually placed near a rigid wall exposed to turbulent flow, recording the sound waves produced by the pressure fluctuations. However, this approach has limitations related to spatial resolution, which is constrained by microphone spacing and configuration. Reducing the spacing between microphones can enhance resolution but often requires more sensors, increasing both cost and setup complexity. Conversely, increasing the distance between sensors may result in the failure to capture all samples of incoming sound waves, leading to a reduction in the resolution of high-frequency pressure fluctuations. Furthermore, the data recorded in this approach can easily be contaminated by background noise and instrument recording noise.

To address these issues, advanced signal processing techniques have been

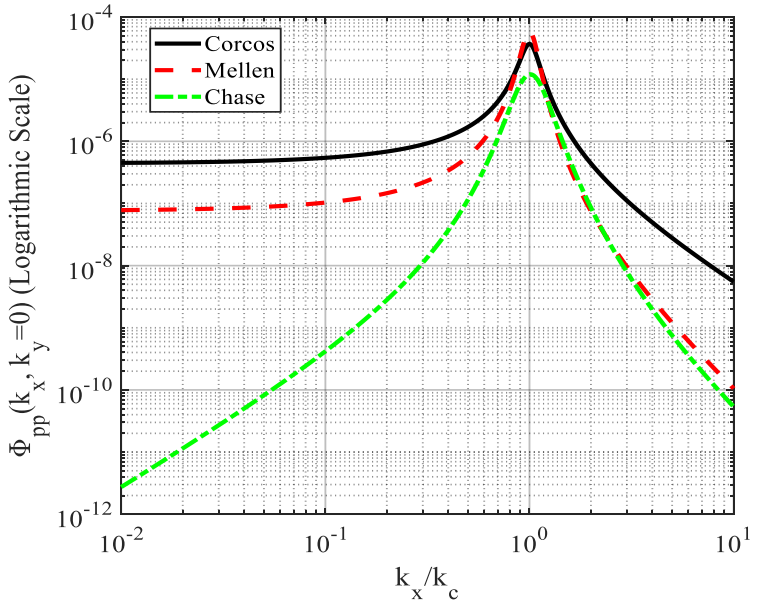

Fig. 2. Wavenumber-frequency spectra for $f = 1000$ Hz as a function of non-dimensional wavenumber for $k_y = 0$ for three semi-empirical TBL models. k_x and k_y represent the streamwise and spanwise wavenumbers, respectively, and k_c is the convective wavenumber.

developed to extract the WPF information [3, 12]. This enables the direct measurement of pressure fluctuations, offering detailed information about the pressure field's characteristics [13]. One widely used signal processing technique is beamforming, which combines microphone outputs to form a directed or focused sensitivity beam. This enhances the desired signal while suppressing interference and noise from other directions. Various beamforming techniques are discussed in [14, 15, 16]. It should be noted that some researchers have used vibration measurements of a structure excited by a TBL to estimate the WPF [17]. However, in this work, we consider only the use of a microphone array, which is the most commonly used method in the literature, with a focus on highlighting challenges on estimation of the low-wavenumber WPF.

Panton and Robert made the initial attempt in using microphones to measure the turbulent wall-pressure spectrum [18]. They utilised only two microphones and increased the distance between them along a line for measuring two-point cross-spectral pressure. This concept had been further expanded to the point that an array of sensors was used for the first time by Maidanik

[19] and was further developed by Blake and Chase [20] and Farabee and Geib [21]. In this approach, the microphones are spaced regularly at specific intervals in a linear streamwise array. Using a linear streamwise equidistant array with intervals of d, they could recognize pressure fluctuations around $k_x = \pi/d$ by analyzing alternate microphone outputs. These mode arrays were then used to calculate spectral levels in sonic and subsonic regions by selecting suitable frequencies [3]. The large surface area of each individual sensor effectively filters out many of the undesired pressure fluctuations associated with convective ridge motions. However, some noises were introduced into the measurement through spatial aliasing [22]. This issue arises due to the finite size of practical sensors and the process of signal averaging over a sensor's surface, which inherently limits the precision of the WPF measurements at high frequencies [23]. Consequently, using larger sensors results in reduced resolution for high-frequency pressure fluctuations. Corcos [24] was a pioneer in exploring the relationship between sensor size and the corresponding spectral attenuation based on theoretical foundations. More recently, Hu [23] introduced a correction model to address high-frequency attenuation associated with sensor size when measuring WPF beneath the TBL.

Aliasing occurs in any array where sensor spacing cannot resolve the smallest turbulent scales [3]. The results of using a large number of sensors were presented by Manoha [25] and Bermer [26] to alleviate the aliasing effect. In order to comprehensively capture the spatial characteristics of the two-point cross-spectrum of the WPF, which can subsequently undergo Fourier transformation to generate the wavenumber-frequency spectrum of wall pressure, an alternative methodology was introduced [27, 28]. In this technique, transducers were deployed in an array spanning the diameter of a disk, arranged along a line that can be rotated to various angular positions. By conducting measurements repeatedly at different rotational orientations of this array, it becomes possible to extract numerous cross-spectral attributes pertaining to the boundary layer. Subsequently, a wavenumber analysis can be conducted to derive valuable insights from the data. The technique of using large arrays and small sensors has enabled investigators to create clear maps illustrating the convective ridge and acoustic cone [29].

It should be noted that a periodic arrangement of microphones is not the best choice since it causes redundant distances between sensors [30]. Various techniques have been proposed to optimize array efficiency. One of the most common techniques is using an array with a spiral shape [31]. The advantage of using a non-equidistant array was studied by Haxter and

Spehr [30] in 2014. They evaluated the efficiency of equidistant and non-equidistant array patterns in detecting a single source in the wavenumber domain. They showed that opposed to the non-equidistant spaced array pattern, the equidistant array has amplitudes on the side lobes identical to that of the main lobe. In other words, the non-equidistant spacing of the transducers has the capability to transfer aliasing effects at a greater wavenumber than in the equidistant array. In addition to Nyquist criterion and array pattern, the co-array size plays an important role in the array performance [3]. Co-array describes the number of different cases where the distance between every pair of sensors is unique [32]. More recently, Schram et al. [33] applied a similar procedure to Ref. [30] and used microphones on a rotatable disk to minimize the number of rotation angles and acquisition time while providing a relatively uniform sampling of the co-array plane.

Beamforming is a powerful technique for enhancing the resolution of sensor arrays, enabling more accurate localization and characterization of sound sources in complex or noisy environments. This method is developed to amplify signals arriving from specific directions. In the context of TBL problems, beamforming is particularly useful for identifying and localizing regions with high levels of WPF and provide valuable insights into the characteristics of turbulent flows. Ehrenfield and Koop [34] were among the pioneers who utilized the beamforming method in their analysis. They measured the WPF beneath a compressible TBL at a high subsonic Mach number using a sparse array of pressure transducers in a wind tunnel. They applied the infinite beamforming technique and deconvolution algorithm to deconvolve the wavenumber-frequency spectrum from the surface pressure array data. They only detect the domains associated with convective peak and acoustic peak in their studies and showed that acoustic noise is particularly dominant in the lower frequencies. In 2017, Haxter et al [35], conducted a study that built upon the work of Ehrefried and Koop [34] by using the same microphone array arrangement to obtain the phase velocity of TBL pressure fluctuations at high subsonic Mach number from wind tunnel data affected by strong background noise. They used a method called CLEAN-SC to remove the dominant existing acoustic signals and their coherent parts in the beamforming map, which improved the accuracy of their results. Additionally, Prigent et al. [36] used beamforming and DAMAS deconvolution techniques to process a synthetic field consisting of a diffuse acoustic field and the Corcos WPF model. To estimate the WPF, they utilized an aligned microphone array with a rotating configuration.

This paper aims to highlight the challenges of using an array of microphones for estimating the low-wavenumber region of TBL wall pressure fluctuations. Most previous studies have primarily focused on identifying the convective ridge and acoustic peak. Moreover, the importance of the low-wavenumber domain in the vibration of structures subjected to turbulent flow as well as the significant discrepancies between different existing TBL models for this region are the main motivations for this work. For this purpose, the study employs a regularized Fourier-based approach (RFBA). This approach relies on the inverse Fourier transform (IFT) expression that links the cross spectrum density (CSD) of the pressure in both physical and wavenumber space. The discretization of the integral in this expression is achieved using the rectangular rule, which results in a linear matrix system. An adapted regularization technique is then used to invert this system and estimate a stable solution. To assess the capability of the RFBA in estimating the low-wavenumber components of the WPF, numerical simulations of a TBL excitation are conducted, and the WPF estimated by the RFBA using a microphone array is compared with the reference WPF of the input TBL model. Considering this process, the effect of number of sensors, array pattern, co-array factor and data averaging on the estimated WPF are examined. Moreover, to mimic experimental measurements, a virtual acoustic experiment is proposed, involving the synthesis of snapshots of the TBL WPF.

The structure of the paper is as follows: Section 2 describes the RFBA, while Section 3 evaluates its effectiveness. Section 3.1 focuses on calculating the CSD matrix of the pressure measured by a virtual microphone array from a closed-from semi-empirical TBL model and particularly studies the effects of three factors of sensor spacing, co-array factor, and sensor distribution on estimation of the WPF in the low-wavenumber domain. In order to simulate real experimental measurements, Section 3.2 estimates the CSD matrix of the pressure measured by the virtual microphone array by averaging different snapshots of the WPF induced by the TBL. These snapshots are generated by employing so-called uncorrelated wall plane wave (UWPW) technique [37]. Performance of the RFBA on estimating the WPF in the low-wavenumber domain is evaluated based on this virtual experiment. The paper concludes with a discussion in Section 4 and a summary of the findings.

2. The Regularized Fourier-based Approach

This section covers the theoretical formulation of the regularized Fourier-based approach to estimate the WPF in the wavenumber domain using pressure measurements obtained from microphones. Fig. 3 shows a network of N_s flush-mounted microphones that are installed on a rigid surface. They are distributed within a rectangular area measuring $L_x \times L_y$. The position of each microphone is determined by the coordinates $\mathbf{x}_i$, denoted as (x_i, y_i) for $i \in \{1, N_s\}$. The sensors are used for recording the WPF beneath a TBL. The TBL is assumed to be homogeneous, stationary and fully developed over the surface. The x-axis is considered parallel to fluid flow with a constant free stream velocity of U_∞.

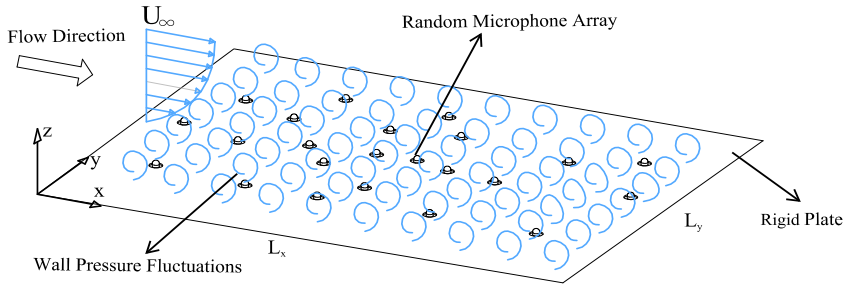

Fig. 3. Schematic representation of a microphone array mounted within a rectangular area with dimensions L_x in length and L_y in width to measure wall pressure fluctuations from the TBL.

The wavenumber-frequency spectrum $\phi_{pp}(k_x, k_y, \omega)$ of the wall pressure $p(x, y, t)$ can be expressed as follows [34]

$$\phi_{pp}(k_x, k_y, \omega) = \frac{1}{4\pi^2} \int_{-\infty}^{\infty} \int_{-\infty}^{\infty} R_{pp}(\xi, \eta, \omega) e^{-\mathrm{j}(k_x \xi + k_y \eta)} \, \mathrm{d}\xi \mathrm{d}\eta, \tag{1}$$

where (ξ, η) are the distances between two points in the (x, y) plane, ω is the angular frequency, $\mathrm{j} = \sqrt{-1}$ is the imaginary unit, and k_x, k_y are wavenumber components in the streamwise and spanwise direction, respectively. $R_{pp}(\xi, \eta, \omega)$ is the temporal Fourier transform of the space-time correlation function of wall pressure given by [34]

$$R_{pp}(\xi, \eta, \omega) = \frac{1}{2\pi} \int_{-\infty}^{\infty} G_{pp}(\xi, \eta, \tau) e^{\mathrm{j}\omega\tau} \, \mathrm{d}t, \tag{2}$$

$$G_{pp}(\xi,\eta,\tau) = \langle p(x,y,t)\, p(x+\xi, y+\eta, t+\tau)\rangle, \tag{3}$$

where the angle bracket $\langle\cdots\rangle$ denotes the mathematical expectation. The IFT of the Eq. (1) can be used to determine how the wavenumber spectrum $\phi_{pp}(k_x, k_y, \omega)$ relates to $R_{pp}(\xi, \eta, \omega)$

$$R_{pp}(\xi,\eta,\omega) = \int_{-\infty}^{\infty}\int_{-\infty}^{\infty} \phi_{pp}(k_x,k_y,\omega) e^{\mathrm{j}(k_x\xi+k_y\eta)}\,\mathrm{d}k_x\mathrm{d}k_y. \tag{4}$$

By employing a rectangular integration method over a truncated wavenumber domain, one can approximate $R_{pp}(\omega)$ between two points $\mathbf{x}_i$ and $\mathbf{x}_j$ as follows

$$R_{pp}(\xi_{i,j},\eta_{i,j},\omega) \approx \sum_{l=1}^{N_k} \phi_{pp}(k_{x,l},k_{y,l},\omega)\, e^{\mathrm{j}(k_{x,l}\xi_{i,j}+k_{y,l}\eta_{i,j})}\,\delta k_x \delta k_y, \tag{5}$$

where $(\xi_{i,j},\eta_{i,j}) = (x_i - x_j, y_i - y_j)$ with $i,j = 1,2,\ldots,N_s$ and $\delta k_x, \delta k_y$ are the wavenumber resolutions in the streamwise and spanwise directions, respectively, and $N_k = N_{k_x} \times N_{k_y}$ corresponds to the total number of grid points in the truncated wavenumber space, and each vector index l is assigned uniquely to a grid point $(k_{x,l}, k_{y,l})$. A cut-off wavenumber is defined to take into account the convective contributions of the TBL WPF (see Section 3). Eq. (5) can be represented in matrix notation as follows

$$\mathbf{S}_{pp} = \mathbf{Q}\Phi_{pp}, \tag{6}$$

where $\mathbf{S}_{pp}$ is a vector consisting of the cross-spectrum elements and Φ_{pp} is a vector consisting of the unknown WPF components in the truncated wavenumber space as follows

$$\mathbf{S}_{pp} = \begin{bmatrix} R_{pp}(\xi_{1,1},\eta_{1,1},\omega) \\ R_{pp}(\xi_{1,2},\eta_{1,2},\omega) \\ \vdots \\ R_{pp}(\xi_{i,j},\eta_{i,j},\omega) \\ \vdots \\ R_{pp}(\xi_{N_s,N_s-1},\eta_{N_s,N_s-1},\omega) \\ R_{pp}(\xi_{N_s,N_s},\eta_{N_s,N_s},\omega) \end{bmatrix}_{N_s^2\times 1}, \mathbf{\Phi_{pp}} = \begin{bmatrix} \phi_{pp}(k_{x,1},k_{y,1},\omega) \\ \phi_{pp}(k_{x,1},k_{y,2},\omega) \\ \vdots \\ \phi_{pp}(k_{x,l},k_{y,l},\omega) \\ \vdots \\ \phi_{pp}(k_{x,N_{k_x}},k_{y,N_{k_y}-1},\omega) \\ \phi_{pp}(k_{x,N_{k_x}},k_{y,N_{k_y}},\omega) \end{bmatrix}_{N_k\times 1} \tag{7}$$

The components of $\mathbf{\Phi_{pp}}$ are organized such that the first N_{k_y} components correspond to $\phi_{pp}(k_{x,1}, k_{y,l}, \omega)$ with $l \in \{1, N_{k_y}\}$, the next N_{k_y} components

correspond to $\phi_{pp}(k_{x,2}, k_{y,l}, \omega)$ with $l \in \{1, N_{k_y}\}$, and so on. Also, for a microphone array with N_s sensors, the elements of $\mathbf{S}_{pp}$ can be measured for the discrete separations of sensors, $(\xi_{i,j}, \eta_{i,j})$, which the first N_s components correspond to $R_{pp}(\xi_{1,j}, \eta_{1,j}, \omega)$ with $j \in \{1, N_s\}$, the next N_s components correspond to $(\xi_{2,j}, \eta_{2,j}, \omega)$ with $j \in \{1, N_s\}$, and so on. Besides, $\mathbf{Q}$ is the matrix with the following elements

$$\mathbf{Q} = \delta k_x \delta k_y \begin{bmatrix} e^{\mathrm{j}(k_{x,1}\xi_{1,1}+k_{y,1}\eta_{1,1})} & e^{\mathrm{j}(k_{x,1}\xi_{1,1}+k_{y,2}\eta_{1,1})} & \dots & \dots & e^{\mathrm{j}(k_{x,N_{k_x}}\xi_{1,1}+k_{y,N_{k_y}}\eta_{1,1})} \\ e^{\mathrm{j}(k_{x,1}\xi_{1,2}+k_{y,1}\eta_{1,2})} & \ddots & & & \vdots \\ \vdots & & & e^{\mathrm{j}(k_{x,l}\xi_{i,j}+k_{y,l}\eta_{i,j})} & \vdots \\ \vdots & & & \ddots & e^{\mathrm{j}(k_{x,N_{k_x}}\xi_{N_s,N_s-1}+k_{y,N_{k_y}}\eta_{N_s,N_s-1})} \\ e^{\mathrm{j}(k_{x,1}\xi_{N_s,N_s}+k_{y,1}\eta_{N_s,N_s})} & \dots & \dots & & e^{\mathrm{j}(k_{x,N_{k_x}}\xi_{N_s,N_s}+k_{y,N_{k_y}}\eta_{N_s,N_s})} \end{bmatrix}_{N_s^2 \times N_k} . \quad (8)$$

Considering Eq. (6), we arrive at N_s^2 equations for the N_k unknown coefficients. In most cases, the number of unknowns N_k exceeds the number of equations N_s^2. Eq. (6) is therefore an under-determined system and the system of equations has no unique solution. Using the Moore-Penrose inverse of matrix $\mathbf{Q}$ can yield a solution with minimal 2-norm, but the problem posed by Eq. (4) is equivalent to a first-kind Fredholm integral equation that is known to be ill-conditioned [38]. Hence, the inversion method derived from the discretization of the Riemann integral formula leads to a severely ill-conditioned linear system (i.e., Eq. (6)) with many tiny singular values. This means applying the Moore-Penrose inversion using singular value decomposition (SVD) generates inadequate results. Since matrix $\mathbf{Q}$ can contain small rounding errors due to computer calculation and vector $\mathbf{S}_{pp}$ can contain errors induced by measurement in practice, the ill-conditioning of $\mathbf{Q}$ can greatly amplify these errors, resulting in erroneous results. However, adapted regularization techniques can produce useful stabilized solutions [38, 39, 40]. The goal of regularization theory is to provide proper side constraints with optimal weights so that the regularized solution is a good approximation of the unknown solution. Different regularization techniques described in [38] were applied to Eq. (6) to evaluate the WPF in the low-wavenumber domain. The truncated generalized singular value decomposition (TGSVD) method with minimising the first derivative 2-norm of the solution was found to be the most appropriate [38, 41]. The regularization parameter is determined from the corner of the discrete L-curve produced by the TGSVD method [42]. For the numerical applications presented herein, the Matlab package developed by C. Hansen for the analysis and solution of discrete ill-posed problems [38] was utilized (See Appendix A).

3. Results and Discussion

To evaluate the WPF in the low-wavenumber domain, the procedure described in Section 2 is employed, and the results obtained by the RFBA are examined.

According to the Graham formulation [43, 44], the CSD of the WPF can be computed using various models for auto-spectral density (ASD) of the pressure field,$\Psi_{pp}(\omega)$, and the normalized CSD of the pressure field, $\tilde{\phi}_{pp}(k,\omega)$, independently from each other as follows

$$\phi_{pp}(\mathbf{k},\omega) = \Psi_{pp}(\omega)\left(\frac{U_c}{\omega}\right)^2 \tilde{\phi}_{pp}(\mathbf{k},\omega). \tag{9}$$

In this work, the ASD function of the WPF is evaluated using the Goody model described in Appendix B (Eq. (B.1)). It should be noted that $\Psi_{pp}(\omega)$ is a one-sided radial frequency spectrum. Therefore, to convert it into cyclic frequency spectrum density $\Psi_{pp}(f)$, $\Psi_{pp}(\omega)$ was multiplied by 2π. For the normalized CSD function, various semi-empirical models have been developed [45]. The Corcos model is by far the most popular model since it considers homogeneity across the surface, and this assumption leads to a cross spectrum model dependent only on the separation distances [9]. Thus, the Corcos model has two separate relationships for representing the in-flow and cross-flow directions of the WPF [9]. Even though separability is convenient analytically, it is not a realistic assumption. Other researchers recognized this issue and proposed a simple change to the Corcos model. For example, Mellen proposed an elliptical coherence zone, which is different from the Corcos model with the rhombic coherence zone [3]. It is well known that Corcos model overpredicts the amplitude of the low-wavenumber domain, whereas the Mellen model provides more realistic predictions of the low-wavenumber levels. This has been confirmed by comparing the vibration responses of a plate excited by a TBL modelled by the Corcos/Mellen models with experimental data [46]. Hence, the Mellen model is used here as the normalized CSD function (see Appendix B, Eq. (B.2)). For all the subsequent numerical analyses, a wavenumber resolution of $\delta k_x = \delta k_y = 4$ m^{-1} is considered and the results are presented at frequency of 1000 Hz.

Furthermore, in order to assess the effectiveness of the proposed method for estimating the WPF in the low-wavenumber domain, we have defined the low-wavenumber domain as the region within the flexural wavenumber ($-k_b \leq k_x, k_y \leq k_b$) of a steel plate with a 1 mm thickness. The plate's

properties include a Young's modulus of 210 Gpa, a density of 7800 (kg m^{-3}), and a Poisson's ratio of 0.3, resulting in a flexural wavenumber of $k_b = 63.26$ m^{-1}. The low-wavenumber region is indicated with the square area in Fig. 4 where the CSD function of the reference TBL using the Goody and truncated Mellen models is plotted. In Section 3.1 and 3.2 we employ the RFBA to estimate the WPF in the low-wavenumber domain and the results are compared with those simulated using the theoretical WPF formula based on the Goody and truncated Mellen models as shown in Fig. 4.

A turbulent flow with an air flow speed of $U_\infty = 50$ m s^{-1} is assumed flowing over the rigid surface, see Fig. 3. The values of air density and the kinematic viscosity are set to 1.225 kg m^{-3} and 1.5111×10^{-5} m^2 s^{-1}, respectively. It is assumed that the TBL is homogeneous, stationary and fully developed over the panel surface. The TBL parameters used for this analysis are given in Table 1. Moreover, the convective velocity U_c is approximated using Bull's model [47, 5] as follows

$$U_c \approx U_\infty \left(0.59 + 0.3e^{-0.89\delta^*\omega/U_\infty}\right), \tag{10}$$

where δ^* is displacement thickness.

The simulations are performed in Matlab on a desktop computer with 32 GB of RAM and four physical cores. To employ Eq. (5), one needs to truncate the wavenumber domain. It is necessary to note that the range of the considered wavenumber domain should be large enough to be able to include the significant contribution of the CSD function. Hence, a cut-off wavenumber of $1.2k_c$ was used in both the streamwise and spanwise directions to take into account the convective contributions of the TBL WPF, where $k_c = \omega/U_c$ is the convective wavenumber. It is noteworthy to mention that converge studies have been done for the selection of the cut-off wavenumber and wavenumber resolution to ensure that the input TBL is accurately modelled.

Table 1. TBL parameters for a air flow with speed of 50 m/s.

Parameter	Value
TBL thickness δ (mm)	5.77
TBL displacement thickness δ^* (mm)	0.729
Wall shear stress τ (pa)	5.989

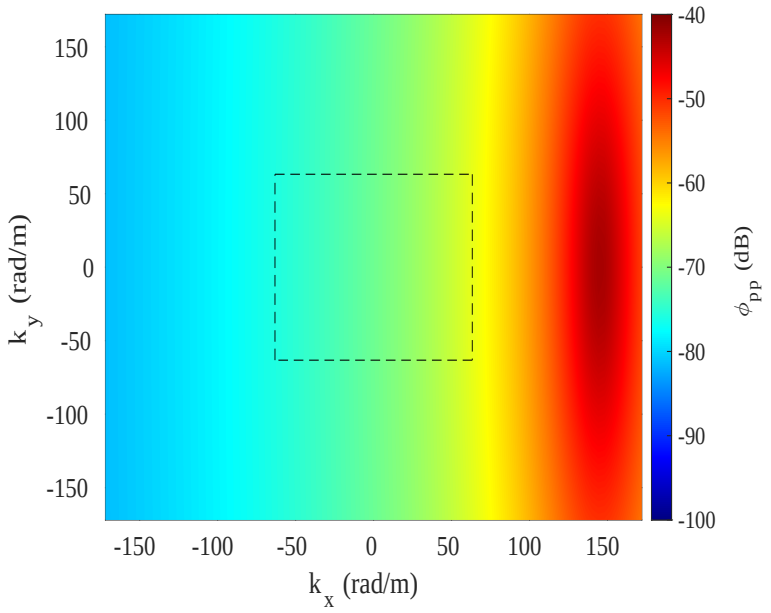

Fig. 4. Contour plots of the Goody+Mellen wavenumber-frequency model for a flow speed of 50 m/s at 1000 Hz.

3.1. ***Effect of Microphone Array Parameters on the Estimated TBL Wall Pressure Field***

In this section, the effects of array parameters namely number of sensors, co-array factor and sensor distribution on the performance of the RFBA are examined. The array size is kept constant in all subsequent calculations.

3.1.1. ***Effect of Sensor Spacing***

Before processing the array data for signal analysis, the initial step involves establishing the relative position of sensors, which is crucial in array creation. In this process, special attention must be given to avoid spatial aliasing. Spatial aliasing arises as a result of spatially under-sampling the aperture of the array. To avoid aliasing in time domain signal processing, it is essential to sample the signal at a rate of at least twice the highest frequency. This sampling rate, known as the Nyquist rate [48], can also be applied in spatial domain signal processing by ensuring that the sampling interval does not exceed one-half wavelength [32]

$$k_{\text{sample}} = 2k_{\text{max}} = \frac{2\pi}{\Delta x}. \tag{11}$$

This equation indicates a direct relationship between the Nyquist waveform frequency and the sampling interval Δx. This interval, as determined by the Nyquist principle, sets a limit on the maximum distance that can exist between microphone positions. As mentioned above, a criterion of 1.2 times of the convective wavenumber is considered for the highest waveform frequency in measuring the pressure with a microphone array. This criterion is taken into account in Eq. (11), so the minimum distance between the microphone positions is obtained as $\Delta x = \pi/k_{\max}$. If this criterion is not fulfilled, then the aliasing can be observed in the low-wavenumber domain, which is the region of interest.

In this section, an equidistant cross-array pattern with the fixed size of $L_x = 455$ mm and $L_y = 375$ mm is assumed to demonstrate the aliasing phenomenon and the effects of sensor spacing on the estimated TBL WPF. The study considers a minimum of 16 sensors, with the number of sensors increased by 4 until the maximum of 68 sensors is reached (as shown in the supplementary document). Fig. 5 presents the results for only four selected cases, namely those with 16, 32, 48, and 68 sensors. As an additional feature, Figs. 5 (c), (g), (k), and (o) demonstrate all possible vector spacings between all pairs of sensors, along with the co-array factors corresponding to each case study. In the upcoming section (Section 3.1.2), the impact of this parameter will be discussed. Fig. 5 (b), (f), (j), and (n) show the color map and Figs. 5 (d), (h), (l), and (p) show the corresponding cross-section view of the estimated WPF obtained by RFBA, respectively, for different number of sensors of cross-array pattern. The color maps in the Fig. 5 include a rectangular area which is surrounded by flexural wavenumber of the assumed plate and denoting the range of low-wavenumber domain which needs to be evaluated ($-k_b \leq k_x, k_y \leq k_b$). This range is shown in the cross-section view of the results with the red dashed-line.

To quantify the performance of the proposed method in the estimation of the TBL WPF, the mean absolute error (MAE) of the estimated WPF in the low-wavenumber domain is calculated for each case with respect to the reference input TBL model based on the Goody and Mellen Models [49, 10] in the corresponding low-wavenumber domain. The following formula is used to compute the MAE of the estimated WPF in the low-wavenumber domain

$$\mathrm{MAE} = \frac{1}{N_{k_{LW}}} \sum_{l=1}^{N_{k_{LW}}} |10\mathbf{log}_{10}\phi_{pp}^{\mathrm{e}}(k_{x,l}, k_{y,l}, \omega) - 10\mathbf{log}_{10}\phi_{pp}^{\mathrm{r}}(k_{x,l}, k_{y,l}, \omega)|, \quad (12)$$

where $N_{k_{LW}}$ corresponds to the total number of grid points in the low-wavenumber domain. $\phi^{\mathrm{e}}_{pp}(k_{x,l}, k_{y,l}, \omega)$ and $\phi^{\mathrm{r}}_{pp}(k_{x,l}, k_{y,l}, \omega)$ are the estimated and reference wavenumber-frequency spectrum of the WPF, respectively. It can be observed from Fig. 5 that by increasing the number of sensors, the estimated WPF is improved, and it gradually converges towards the reference input TBL model (see, Fig. 4).

It is clear from Figs. 5 (f) and (h) that RFBA struggle to provide reasonable estimation of the WPF due to the presence of aliasing phenomenon when $N_s < 48$. For the given array size, the aliasing effect is mitigated by increasing the number of sensors to 48. This is consistent with Nyquist criterion, as for the considered array size, according to Eq. (11) at least 24 sensors are required along the x-axis and 20 sensors along the y-axis to satisfy the Nyquist criterion and avoid aliasing effect. Assuming that the number of sensors is the same in both the streamwise and spanwise directions, the minimum number of sensors required to satisfy the criterion is $N_s = 48$ which is what we observed in Figs. 5 (j) and (i). An interactive plot demonstrating the impact of increasing the number of sensors on reducing the aliasing effect is shown in Fig. S1 of the supplementary document.

As illustrated by Figs. 5 (j) and (n) and their corresponding MAEs, the accuracy of estimated results is improved by increasing the number of sensors from 16 to 48, but adding more sensors does not significantly enhance the estimated WPF in the low-wavenumber domain (see Figs. 5 (j) and (n)). This suggests that respecting the Nyquist criterion alone is not sufficient for obtaining accurate estimation of the low-wavenumber WPF. However, this does not hold true for the convective region. Fig. 5 (h) shows that estimation of the convective region is much easier than the low-wavenumber domain as it has the highest amplitude in the domain. Moreover, a good estimation of this region is achieved using only 24 sensors which does not satisfy the Nyquist criterion (see Fig. S1) and the estimated result in this region is quite accurate when the Nyquist criterion is fulfilled. Therefore, unlike the low-wavenumber region, accurate estimation of the convective region is possible by fulfilling only the Nyquist criterion.

Figs. 5 (c), (g), (k), and (o) also show that the co-array factor F is always below 0.4 for all the sensor spacing using the equidistant cross array. The effect of this parameter is examined in the following section.

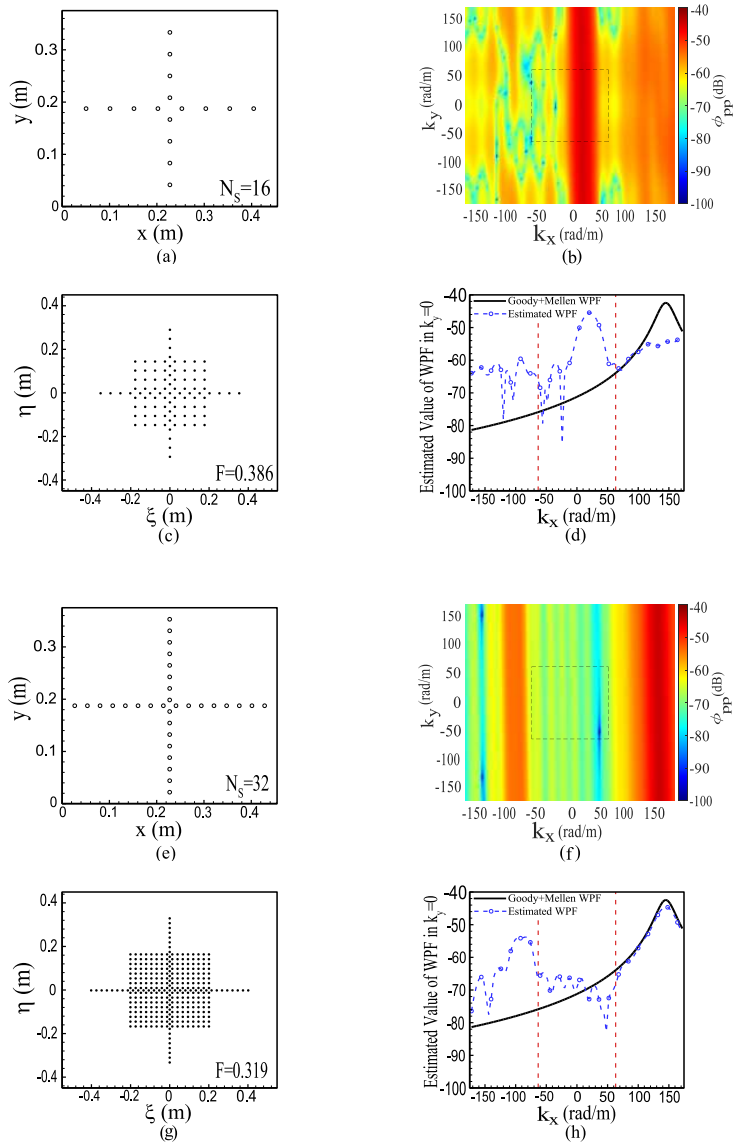

Fig. 5 - Part 1. Comparison of the estimated WPF using RFBA for equidistant cross-array pattern with 16 (a-d) and 32 (e-h) sensors, respectively. Equidistant cross arrays for each case are shown in (a) and (e) and associated set of distinct vector spacings between sensors are presented in (c) and (g). Co-array factor (F) are displayed for each case and MAEs calculated between the reference input TBL model and the estimated low-wavenumber WPF shown in (b) and (f) are 13.48 dB and 5.67 dB, respectively. 2D wavenumber-frequency spectra for $k_y = 0$ are plotted against longitudinal wavenumber in (d) and (h).

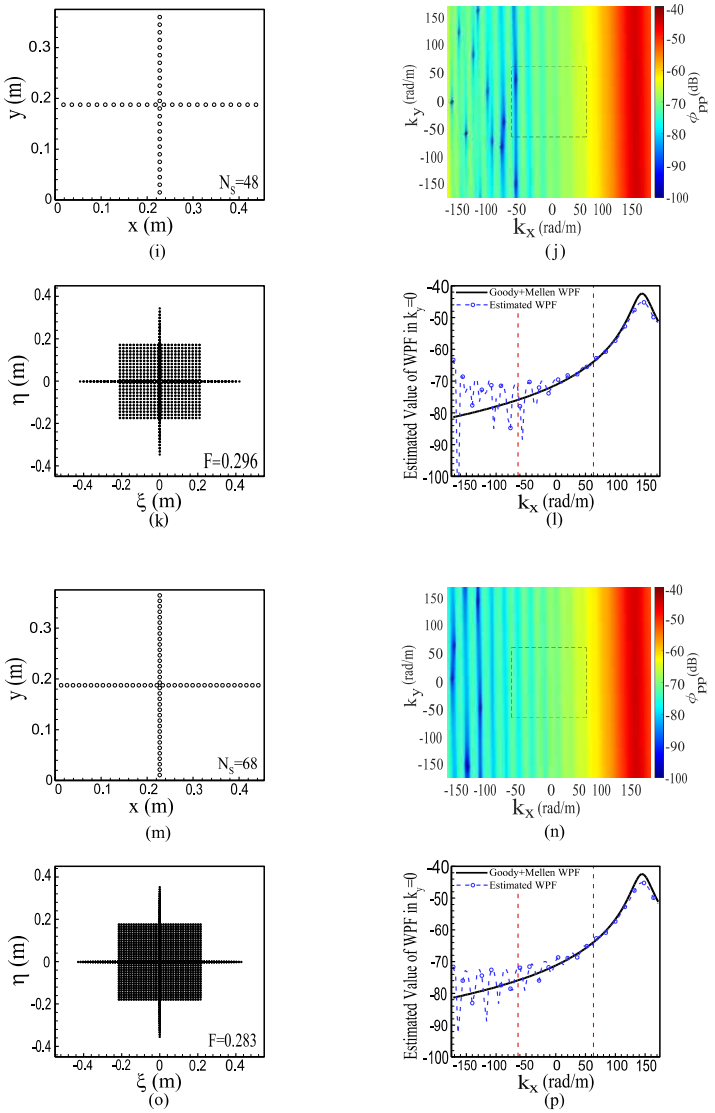

Fig. 5 - Part 2. Comparison of the estimated WPF using RFBA for equidistant cross-array pattern with 48 (i-l) and 68 (m-p) sensors, respectively. Equidistant cross arrays for each case are shown in (i) and (m) and associated set of distinct vector spacings between sensors are presented in (k) and (o). Co-array factor (F) are displayed for each case and MAEs calculated between the reference input TBL model and the estimated low-wavenumber WPF shown in (j) and (n) are 1.81 dB and 1.49 dB, respectively. 2D wavenumber-frequency spectra for $k_y = 0$ are plotted against longitudinal wavenumber in (l) and (p).

3.1.2. ***Effect of Co-array Factor***

In terms of array performance, in addition to the minimum distance between sensors, the size of co-array is an important factor to be considered. Co-array describes the number of different distances between every pair of sensors in the array [3]. Given an array of N_s sensors whose locations are given by

$$\mathbf{x}_m, \quad m = 1, 2, \ldots, N_s. \tag{13}$$

The associated set of vector spacing between all pairs of elements in the array can be expressed as

$$\mathbf{X}_p = \mathbf{x}_m - \mathbf{x}_n, \quad m = 1, 2, \ldots, N_s, \quad n = 1, 2, \ldots, N_s. \tag{14}$$

The set of points $\mathbf{X}_p$ is called the co-array of the array $\mathbf{x}_m$ [50]. To evaluate the efficiency of the different periodic array pattern with respect to aperiodic ones, the F factor is introduced below, which show the ratio of the actual number of unique vector spacings of an array, P, to the corresponding maximum number of spacings, $P_{\max}$

$$F = \frac{P}{P_{\max}} \leq 1. \tag{15}$$

Since there are N_s^2 vectors, and N_s of these are zero, the maximum possible unique vector spacings in an array consisting of N_s sensors can be calculated as follow

$$P_{\max} = N_s^2 - (N_s - 1)\,. \tag{16}$$

An optimal array maximizes the number of unique vector spacings, resulting in $F = 1$. The low value of F means that there will be a large number of duplicate distances between the sensors, which usually can be seen in the periodic pattern. For instance, in Figs. 5 (c), (g), (k) and (o), the F factor decreases with an increase in the number of sensors. This indicates that when more sensors are added in a cross-array pattern at equal distances, the size of P will not increase as much as $P_{\max}$ (Eq. (16)) due to the repetitive occurrence of the same distances. Thus, it can be inferred that improper sensor positioning can lower the F factor. This is one of the reasons why an accurate WPF estimate in the low-wavenumber domain cannot be obtained by equidistant cross array pattern even with 68 sensors (see Figs. 5 (n) and (p)).

To maximize the co-array size while using a fixed number of sensors, it is generally preferable to opt for a non-equidistant arrangement of the array. This will result in a relatively low level of secondary lobes on the estimated WPF, which appear due to the aliasing effect [32]. In the following, the effect of the non-equidistant cross-array pattern on estimation of the WPF is studied.

To maximize F factor in the cross-array pattern, the position of sensors are arranged non-equidistantly on the two cross lines, and the same study as above (Section 3.1.1) has been carried out again. Fig. 6 presents the results with the same number of sensors as studied in Section 3.1.1. Similar to the equidistant-array pattern, the convective region is the first region where the estimated WPF converges to the reference model. However, in the non-equidistant array pattern, only 16 sensors are required to identify this region (Figs. 6 (b) and (d)), whereas in the equidistant array pattern, it takes at least 24 sensors (see Fig. S1). Moreover, the estimated WPF obtained by the RFBA in each case (Figs. 6 (b), (f), (j), and (n)) is more accurate than corresponding case in the equidistant cross-array pattern (Figs. 5 (b), (f), (j), and (n)), which is evident by the lower MAE for the non-equidistant array. As it can be seen from Figs. 6 (f) and (h), in this case the aliasing effect is less profound for the array with 32 sensors when compared to the corresponding case shown in Figs. 5 (f) and (h). Consequently, this improvement results in a decrease in the MAE from 5.07 dB to 3.03 dB.

In the supplementary document, readers can access an interactive plot (Fig. S2) that showcases how WPF estimation in the low-wavenumber domain is affected by 14 arrays of non-equidistant cross-array patterns. The plot includes the results for different arrays from 16 to 68 sensors, with increments of 4.

Comparing the results presented in Figs. 5 and 6, it can be concluded that respecting the Nyquist criterion and the maximum co-array factor can result in a better estimation of the WPF. In the next section, it is demonstrated that in addition to sensor spacing and co-array factor, sensor distribution plays a key role in accurate estimation of the TBL WPF. Effect of this factor has been investigated using a random array pattern in the following section.

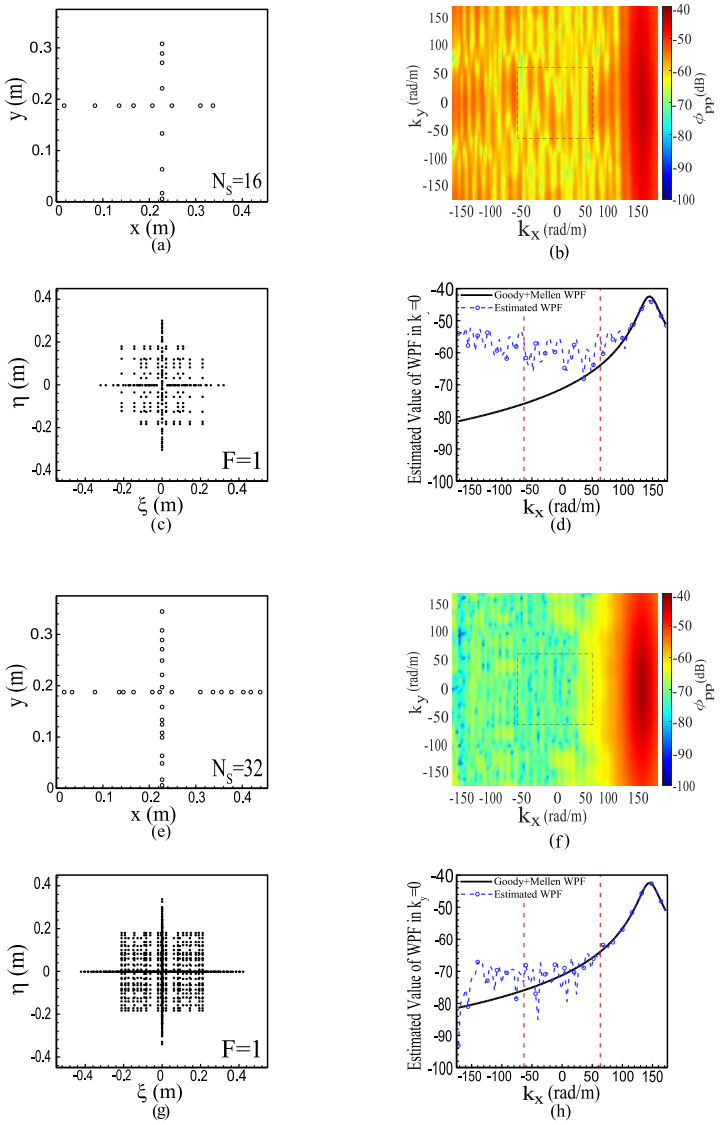

Fig. 6 - Part 1. Comparison of the estimated WPF using RFBA for non-equidistant cross-array pattern with 16 (a-d) and 32 (e-h) sensors, respectively. Non-equidistant cross arrays for each case are shown in (a) and (e) and associated set of distinct vector spacings between sensors are presented in (c) and (g). Co-array factor (F) are displayed for each case and MAEs calculated between the reference input TBL model and the estimated low-wavenumber WPF shown in (b) and (f) are 10.63 dB and 3.03 dB, respectively. 2D wavenumber-frequency spectra for $k_y = 0$ are plotted against longitudinal wavenumber in (d) and (h).

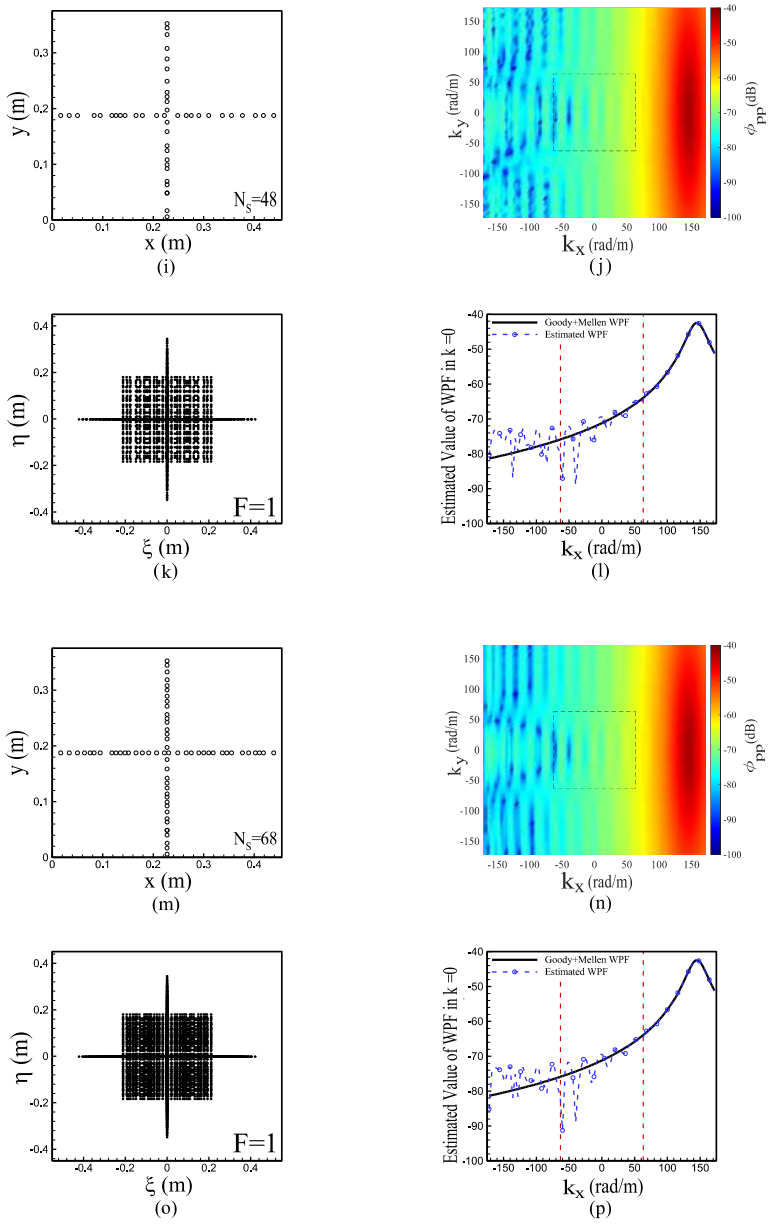

Fig. 6 - Part 2. Comparison of the estimated WPF using RFBA for non-equidistant cross-array pattern with 48 (i-l) and 68 (m-p) sensors, respectively. Non-equidistant cross arrays for each case are shown in (i) and (m) and associated set of distinct vector spacings between sensors are presented in (k) and (o). Co-array factor (F) are displayed for each case and MAEs calculated between the reference input TBL model and the estimated low-wavenumber WPF shown in (j) and (n) are 1.45 dB and 1.31 dB, respectively. 2D wavenumber-frequency spectra for $k_y = 0$ are plotted against longitudinal wavenumber in (l) and (p).

3.1.3. ***Effect of Sensor Distribution***

As discussed above, the half-wavelength criterion is the main constraint of regular array patterns. Failure to meet this criterion, results in spatial aliasing, which produces secondary lobes on the estimated WPF as it was illustrated in Figs. 5 (b) and (f). It is possible to diminish these secondary lobes by removing all periodicities from the microphone array. This results in a class of arrays known as irregular or aperiodic arrays [32].

In order to design an irregular array, a random process can be used to determine sensor locations. Another option would be to use an algorithm that ensures a certain degree of irregularity in sensor positions. The latter should be used whenever a sensor location can be specified and controlled because a knowledge-based sensor location approach outperforms a random algorithm [32]. In this work, the second approach is employed for distributing the sensors and creating a random-array pattern. Fig. 7 shows the estimated WPF using the RFBA for four random array patterns with the number of sensors of 16, 32, 48, and 68. For additional visualization, an interactive plot (Fig. S3) containing 14 random array patterns with sensors ranging from 16 to 68 in increments of 4 is available in the supplementary document. All the configurations meet the Nyquist criterion and have the maximum possible co-array factor (i.e. $F = 1$). For example, for the first irregular array of 16 sensors, the sensor arrangement was designed such that at least one pair of sensors satisfied the Nyquist criterion in both the streamwise and spanwise directions. Following this, in each subsequent step, four new sensors were added to the previous arrangement in such a way that at least one existing sensor could meet the minimum distance required by the Nyquist criterion for each new sensor. This process was repeated up to the fourteenth array of 68 sensors. Also, the position of sensors was chosen in a manner that the F factor was always maximi and equal to 1. The obtained results in Fig. 7 show that using the irregular array with above conditions will avoid spatial aliasing and also generate a more coherent vector spacing separation of ξ and η which lead to the better estimation of the WPF compared with the regular array patterns.

Fig. 7 shows that using the irregular array the estimated WPF converges to the reference WPF much faster than that using the regular array. For example, Figs. 7 (j) and (l) show that applying RFBA to a random array with 48 sensors provides excellent estimations of the WPF in the low-wavenumber domain with a mean absolute error of less than 1 dB. Moreover, RFBA

provides an accurate result in the entire considered wavenumber domain using 68 sensors (shown in Figs. 7 (n) and (p)). Therefore, employing a random array pattern while adhering to the Nyquist criterion and optimizing the co-array factor yields improved WPF estimations in comparison to the other array patterns investigated in Sections 3.1.1 and 3.1.2. In Section 3.1, we used a closed-from semi-empirical TBL model for computing the CSM. However, in practice, only limited number of samples/snapshots of the WPF is available. To investigate the impact of this factor on the proposed RFBA method, we introduce a virtual acoustic experiment, which we examine in detail in the subsequent section.

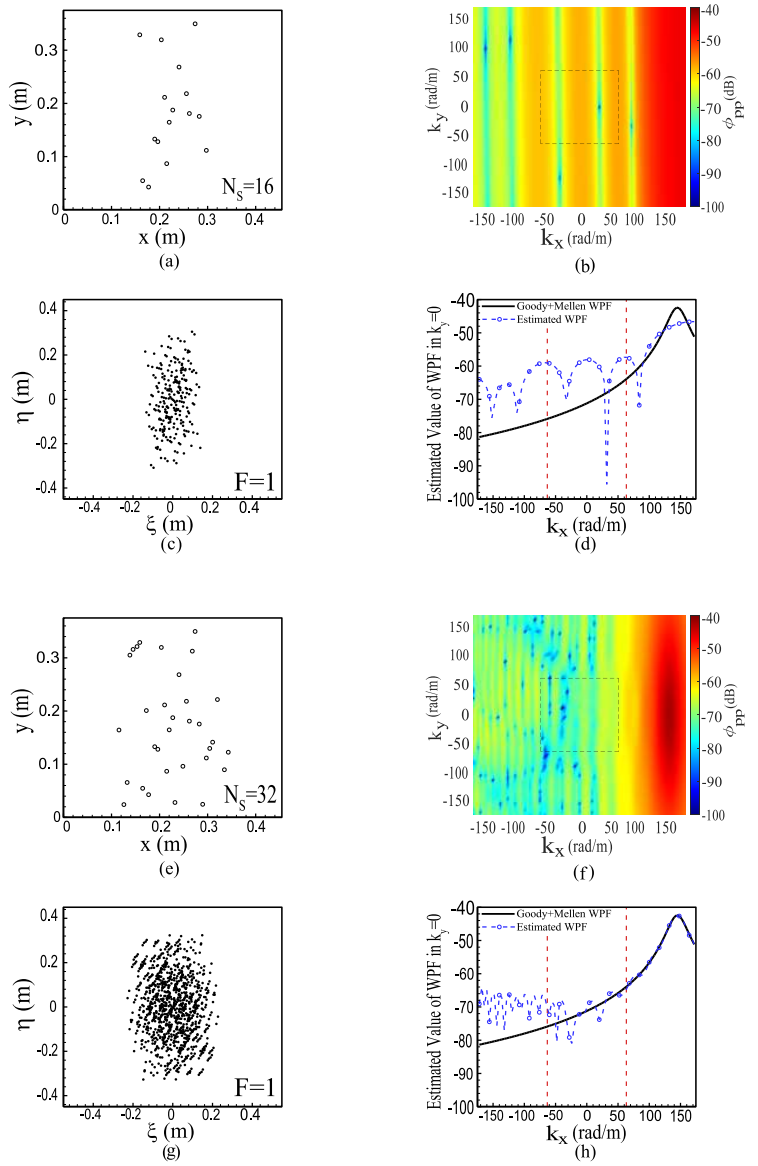

Fig. 7 - Part 1. Comparison of the estimated WPF using RFBA for irregular-array pattern with 16 (a-d) and 32 (e-h) sensors, respectively. Irregular arrays for each case are shown in (a) and (e) and associated set of distinct vector spacings between sensors are presented in (c) and (g). Co-array factor (F) are displayed for each case and MAEs calculated between the reference input TBL model and the estimated low-wavenumber WPF shown in (b) and (f) are 10.08 dB and 2.68 dB, respectively. 2D wavenumber-frequency spectra for $k_y = 0$ are plotted against longitudinal wavenumber in (d) and (h).

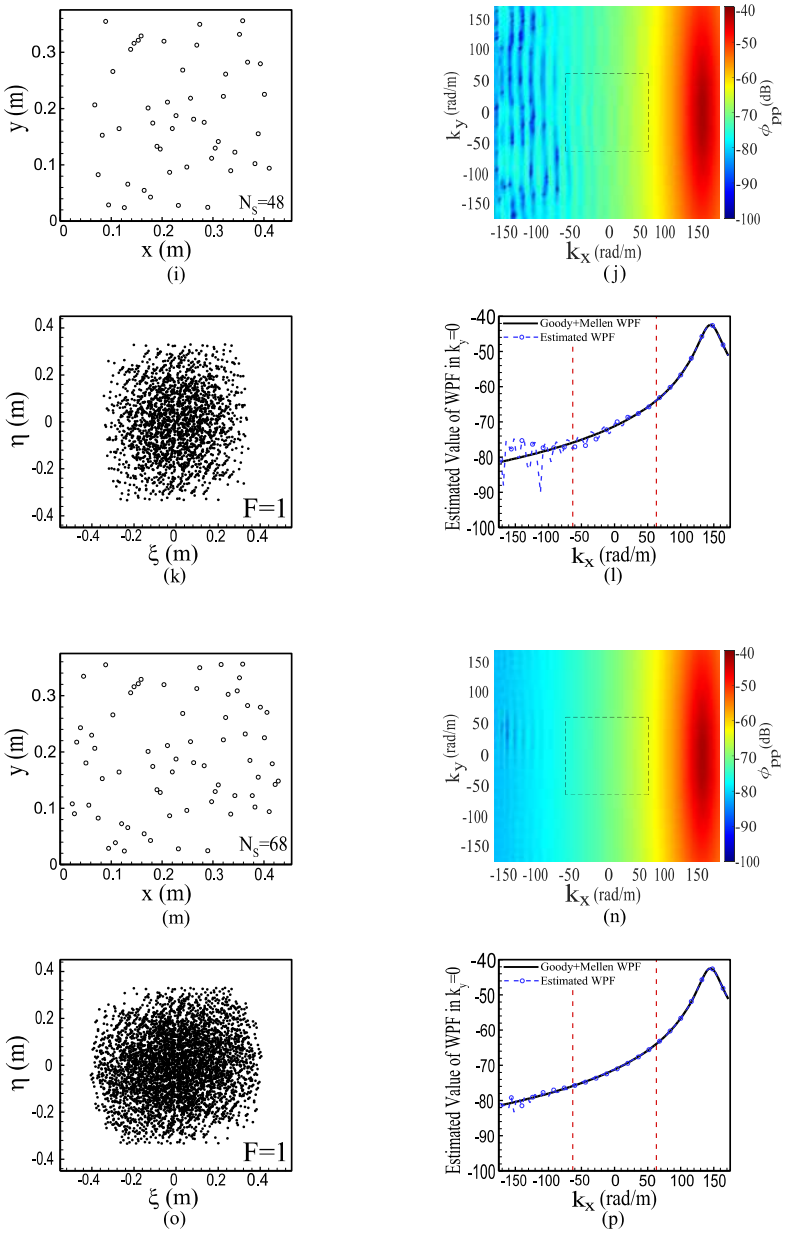

Fig. 7 - Part 2. Comparison of the estimated WPF using RFBA for irregular-array pattern with 48 (i-l) and 68 (m-p) sensors, respectively. Irregular arrays for each case are shown in (i) and (m) and associated set of distinct vector spacings between sensors are presented in (k) and (o). Co-array factor (F) are displayed for each case and MAEs calculated between the reference input TBL model and the estimated low-wavenumber WPF shown in (j) and (n) are 0.61 dB and 0.09 dB, respectively. 2D wavenumber-frequency spectra for $k_y = 0$ are plotted against longitudinal wavenumber in (l) and (p).

3.2. ***Virtual Acoustic Experiments***

In the previous sections, the CSM was calculated from a closed-from semi-empirical TBL model. It was then utilized to investigate the effects of sensor spacing, co-array factor and sensor distribution on the performance of the RFBA in estimation of the WPF in the low-wavenumber domain. However, the theoretical TBL models cannot realistically simulate an experimental situation. Since the TBL pressure fluctuation is a random process, if several records of these pressure fluctuations are taken under the same experimental conditions, they would not be identical due to the random nature of the excitation. Each outcome of an experiment, in the case of a random process, is called a sample function. If n experiments are conducted, all the n possible outcomes of a random process constitute what is known as the ensemble of the process.

In this section, this process is simulated using a virtual acoustic experiment where different deterministic realizations of the TBL pressure fluctuations are computed, and the CSM is then estimated from ensemble average of these realizations.

3.2.1. Wall Pressure Field Snapshots using the UWPW Technique

Simulation of random TBL with deterministic loading is the main concept of the UWPW technique [37]. This approach mimics experimental conditions and calculates the WPF underneath of a TBL by ensemble averaging of the different realization of wall pressure at each frequency. The pressure beneath the TBL for the rth realization can be represented by a set of UWPWs at the qth sensor of the array pattern as follows [46, 37, 51]

$$p^r(\mathbf{x}^q,\omega)=\sum_{l=1}^{N_k}\sqrt{\frac{\phi_{pp}(k_{x,l},k_{y,l},\omega)\delta k_x\delta k_y}{4\pi^2}}e^{\mathrm{j}(k_{x,l}x^q+k_{y,l}y^q+\theta_l^r)}, \tag{17}$$

where θ is a random phase uniformly distributed in $[0,2\pi]$. Similar to Eq. (5), N_k corresponds to the total number of grid points in the truncated wavenumber space. It is important to note that a cut-off wavenumber of $1.2k_c$ was employed in both the streamwise and spanwise directions to consider the convective contributions of the TBL WPF. As an illustration, Fig. 8 displays the representation of four realizations of the surface pressure filed at a frequency of 1000 Hz and a flow velocity of 50 m/s. These realizations are employed in ensemble averaging of different realizations to compute the CSM of the WPF. Fig. 9 shows a flowchart describing the implementation

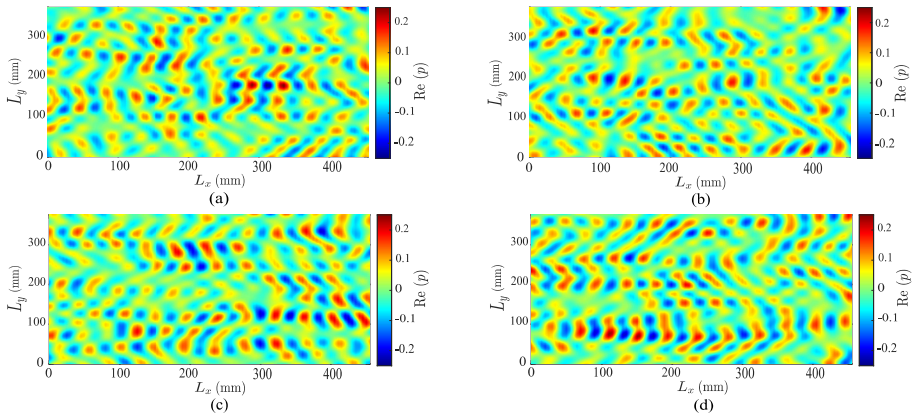

Fig. 8. (a)-(d): Four different realizations of the WPF synthesized by the UWPW technique using the Goody and truncated Mellen models for a flow speed of 50 m/s at 1000 Hz.

of the UWPW technique in the virtual acoustic experiment for estimation of the WPF in the low-wavenumber domain.

Herein, three patterns (equidistant-cross array, non-equidistant-cross array, and irregular array) with 68 sensors are analyzed, and the impact of varying the number of realizations on estimating the WPF in the low-wavenumber domain using the RFBA is evaluated. The supplementary document contains an interactive plot showcasing 19 case studies for the three array patterns, highlighting the impact of varying numbers of realizations on estimation of the WPF in the low-wavenumber domain (see Fig. S4). Besides, for each array pattern, the MAE is shown to help quantifying the accuracy of the estimated WPF for different realizations. Fig. 10 only shows some selected results for four different number of realizations. The obtained results shown

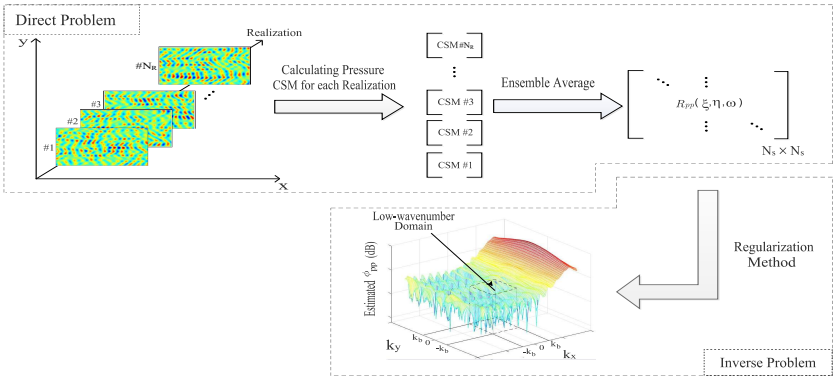

Fig. 9. Simulation process in the virtual acoustic experiments using the UWPW technique.

in Figs. 10 (f1) and (i1), indicate that a relatively small number of realizations is sufficient to identify the convective zone of the WPF in this virtual experiment and the random array pattern exhibits a better performance compared with the other two arrays shown in Figs. 10 (d1), (g1), (e1) and (h1). However, for the estimation of the WPF in the low-wavenumber domain, a considerable number of realizations is necessary. For example, Fig. 10 (f2) shows that after 50000 realizations, the estimated results has a MAE of approximately 4.5 dB. Moreover, increasing the number of realizations from 50000 to 200000 reduces the MAE by only 1 dB (see Fig. 10 (l2)). This can be attributed to the fact that in the virtual experiment an approximate CSM is used which struggles to realise the pressure fluctuations in this region due to their low amplitudes compared to the convective region. Moreover, the MAE values for three different patterns indicate that the irregular-array pattern performs better than the equidistant and non-equidistant cross array patterns when evaluating the WPF in the low-wavenumber domain.

To analyze the WPF synthesized with Eq. (17), the coherence obtained from the WPF of N_R realizations are compared with the coherence obtained from the Mellen+Goody model's analytical formula in Fig. 11. By using N_R realizations, the coherence between point $\mathbf{x}$ and $\mathbf{x}'$ can be estimated as follows

$$\Gamma(\mathbf{x},\mathbf{x}',\omega) = \frac{\left| E\left[p^r(\mathbf{x},\omega)\overline{p^r(\mathbf{x}',\omega)} \right]_{r\in\{1,\dots N_R\}} \right|}{\sqrt{E\left[\left|p^r(\mathbf{x},\omega)\right|^2 \right]_{r\in\{1,\dots N_R\}} E\left[\left|p^r(\mathbf{x}',\omega)\right|^2 \right]_{r\in\{1,\dots N_R\}}}}, \tag{18}$$

where $p^r(\mathbf{x},\omega)$ is given by Eq. (17).

Fig. 11 shows the results of Eq. (18) for $N_R = 50, 500, 5000$, and $N_R = 50000$ when applied to the 34 equidistant sensors positioned in the streamwise direction. It can be observed that a relatively small number of realizations is sufficient to estimate the coherence of the WPF between closely spaced sensors, which plays a vital role in calculating the convective peak in the WPF. However, there are significant discrepancies between the estimated coherence and the analytical one for sensors that are spaced far apart. By increasing the number of realizations, the estimated coherence for sensors with larger spatial separation approaches the analytically calculated coherence, which is crucial for accurate WPF estimation in the low-wavenumber range. This behaviour clarifies why a large number of realizations is necessary to estimate the WPF in the low-wavenumber range.

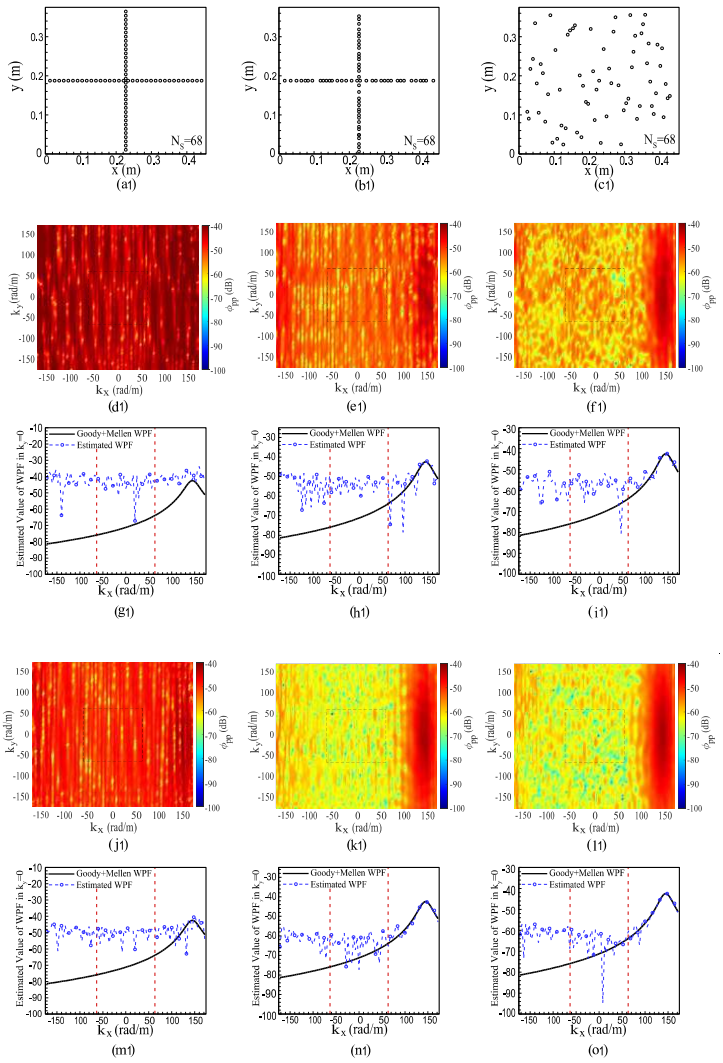

Fig. 10 - Part 1. Comparison of the estimated WPF using the UWPW technique for three different array patterns, each comprising 68 sensors shown in (a1)-(c1) for 500 realizations (d1-i1) and 5000 realizations (j1-o1). The color maps depicting the estimated WPF are presented in (d1), (e1), (f1), (j1), (k1), and (l1), with respective MAEs between the reference input TBL model and the estimated low-wavenumber WPF of 26.86 dB, 16.20 dB, 12.90 dB, 20.12 dB, 8.01 dB, and 7.48 dB. The cross-section view of the estimated low-wavenumber WPF are illustrated in (g1), (h1), (i1), (m1), (n1), and (o1).

582

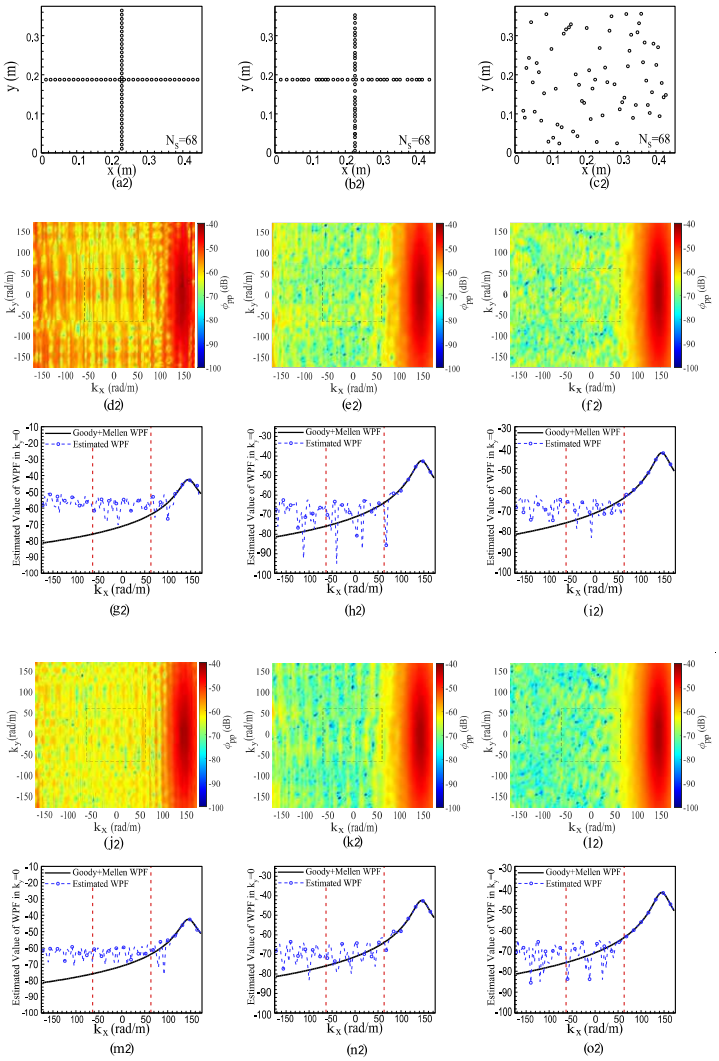

Fig. 10 - Part 2. Comparison of the estimated WPF using the UWPW technique for three different array patterns, each comprising 68 sensors shown in (a2)-(c2) for 50000 realizations (d2-i2) and 200000 realizations (j2-o2). The color maps depicting the estimated WPF are presented in (d2), (e2), (f2), (j2), (k2), and (l2), with respective MAEs between the reference input TBL model and the estimated low-wavenumber WPF of 10.80 dB, 4.65 dB, 4.55 dB, 8.37 dB, 4.22 dB, and 3.39 dB. The cross-section view of the estimated low-wavenumber WPF are illustrated in (g2), (h2), (i2), (m2), (n2), and (o2).

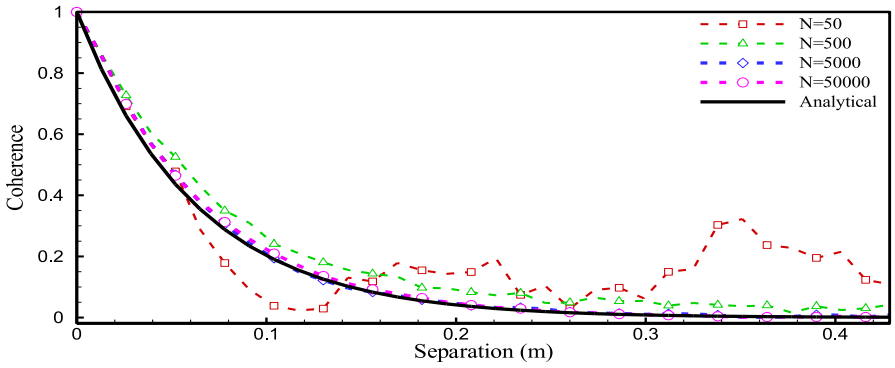

Fig. 11. The TBL pressure filed coherence as a function of the spatial separation in the streamwise direction. Solid line, analytical formula of the Mellen+Goody model; dashed lines, numerical estimation considering $50, 500, 5000$ and 50000 realizations.

3.2.2. ***Effect of the Convective Ridge on the Estimation of the Low-wavenumber WPF***

In previous Sections, we exclusively utilized the Mellen model as the input TBL model. Since the levels of the WPF between the convective peak and the low-wavenumber domain are different for different semi-empirical models (see Fig. 2), in this section we investigate how this difference will affect the estimated low-wavenumber WPF. Hence, we have implemented two additional models: the Chase model [11, 44] and the Corcos model [9, 44], as input TBL models. As can be seen from Fig. 2, among these three models, the levels of low-wavenumber WPF are the highest for Corcos model and the lowest for Chase model while they are somewhere in between for the Mellen model. The disparities between the convective peak level and the mean value of the WPF within the low-wavenumber domain are approximately 19 dB, 27 dB and 33 dB for the Corcos, Mellen and Chase models, respectively. In both the Corcos and Chase models, the convective peak occurs at a similar level as observed in the Mellen model [44].

For the estimation of the WPF, we employed a random array pattern with 68 sensors, as shown in Fig. 10 (c1). We calculated the MAE for the three TBL models with different numbers of realizations, and the results are summarized in Table 2. The findings indicate that when using the Corcos model, fewer realizations are required for an accurate estimation of the WPF within the low-wavenumber domain. In fact, with just 50,000 realizations, we can achieve WPF estimation with a MAE of approximately 2 dB. This number

Table 2. MAE of the low-wavenumber WPF for multiple numbers of realizations using three closed-form semi-empirical models as reference input TBL models.

Semi-empirical models	**Number of Realizations**							
	500	**5,000**	**50,000**	**200,000**	**500,000**	**700,000**	**1,000,000**	**2,000,000**
MAE (dB) - Corcos Model	6.19	3.39	2.18	1.36	0.60	0.51	0.48	0.32
MAE (dB) - Mellen Model	12.90	7.48	4.55	3.39	2.72	2.61	2.19	2.03
MAE (dB) - Chase Model	26.06	20.31	15.97	13.87	11.27	11.14	10.59	9.34

of realizations is significantly fewer than what is needed for the Mellen model (nearly 1,000,000 realizations) to reach the same level of accuracy. This can be attributed to the fact that the difference between the convective peak and the low-wavenumber levels in the Corcos model is smaller than that in the Mellen model. Therefore, the low-wavenumber components of the WPF are less contaminated by the convective ridge. Consequently, a lower number of realizations is necessary to attain an accurate estimation of the WPF within the low-wavenumber domain.

This has been further confirmed by the results for the Chase model where its MAE exceeds that of the Mellen model. For example, when using the Chase model, to achieve WPF estimation with approximately 9 dB error, almost 2,000,000 realizations are required. Since the disparity in the WPF levels between the convective peak and the low-wavenumber domain is the highest for the Chase model among the considered models, the low-wavenumber components of the WPF are mostly masked by the large-amplitude components of the WPF in the convective ridge. This is one of the main challenges of measuring the low-wavenumber pressure fluctuations using a microphone array in real-world scenarios as the difference between the convective peak and low-wavenumber levels of the WPF is not known. This means it is not clear how many snapshots of the measured signal is required to achieve an accurate estimation of the low-wavenumber region.

It should be noted that in this virtual experiment the effect of data sampling and using an approximate CSM on the estimation of the TBL pressure field is demonstrated which is only one aspect of a real experiment. However, other common sources of error including instrumental, environmental, procedural, and human errors exist in practice. These errors can be either random or systematic, impeding the accurate estimation of the WPF in the low-wavenumber domain.

4. Conclusions

In this work, the efficacy of using a microphone array on the estimation of the TBL WPF in the low-wavenumber domain was studied. A regularized Fourier-based approach was proposed to identify the low-wavenumber levels of the WPF. Effects of three array parameters, namely sensor spacing, co-array factor and sensor distribution on the performance of each method were examined. It was shown that to achieve accurate estimation of the WPF all the three factors should be considered. It was found that to obtain accurate results, in addition to the Nyquist criterion, one needs to use an irregular array pattern with the maximum possible co-array factor ($F = 1$). It was also observed that reasonable estimation of the WPF in the convective region is much easier than that in the low-wavenumber domain and can be achieved with relatively small number of sensors.

Moreover, the effectiveness of using a microphone array to estimate the WPF in an experimental condition was evaluated using a virtual experiment where the CSM was approximated by an ensemble average of different realization of the WPF generated by the UWPW technique. This mimics an experimental measurement where many samples are collected from the random TBL pressure fluctuations. It was illustrated that increasing the number of realizations results in more accurate estimation of the wall pressure spectrum. Although, with relatively small number of realizations the convective region can be identified, a significant number of realizations is required to well estimate the low-wavenumber levels in the TBL pressure field.

To investigate the effect of the convective ridge on the identification of the low-wavenumber domain WPF, three different TBL models were used individually as input reference models. It was observed that the difference between the convective peak and the low-wavenumber levels significantly affects the accuracy of low-wavenumber WPF estimation. In other words, the greater this difference, the higher the number of realizations. This happens because the convective ridge obscures the low-wavenumber components of the TBL WPF. This underscores a key issue when trying to capture the low-wavenumber pressure fluctuations using a microphone array in real-world scenarios, as the exact difference between the convective peak and the low-wavenumber levels is unknown in practice. As a result, it remains unclear how many snapshots of the recorded signal are required to achieve an accurate estimation of the low-wavenumber region. Moreover, this highlights the challenges in estimation of this region in the experiments where not only

a limited number of data samples can be recorded but also there are many different sources of error and uncertainties such as background noise, instrumental and human error.

Acknowledgements

The first author acknowledges that this research is supported by UTS President's Scholarship.

Appendix A. TGSVD method

Using Eqs. (5) and (8), one can calculate the vector $\mathbf{S}_{pp}$ and matrix $\mathbf{Q}$. To obtain the best estimation of the WPF components, the following steps from Ref. [38] are employed:

Step 1: compute discrete first derivative operators;

```
L=get_l(size(Q,2),1);
```

Step 2: Compute the compact generalized SVD of a matrix pair;

```
[UU,sm,XX]=cgsvd(Q,L)
```

Step 3: Compute all TGSVD solutions;

```
k_tgsvd=1:size(sm,1)
[X_tgsvd,Rho,Eta]=tgsvd(UU,sm,XX,Sp,k_tgsvd);
```

Step 4: Find the corner of a discrete L-curve via an adaptive pruning algorithm;

```
k_corner=corner(Rho,Eta)
```

Step 5: Find the estimated WPF components for the optimal regularization parameter obtained from the corner method;

```
Phipp=X_tgsvd(:,k_corner)
```

Appendix B. ASD function and normalized CSD function

The Goody model: The empirical model of the ASD function of the pressure field is given by [49]

$$\Psi_{pp}(\omega) = \frac{3\tau_\omega^2 \delta \left(\frac{\omega\delta}{U_e}\right)^2}{U_e \left(0.5 + \left(\frac{\omega\delta}{U_e}\right)^{0.75}\right)^{3.7} \left(1.1 R_T^{-0.57} \left(\frac{\omega\delta}{U_e}\right)\right)^7} \tag{B.1}$$

where $R_T = U_\tau^2 \delta / U_e \nu$ and U_e is the boundary layer edge velocity.

The Mellen model: The Mellen normalized wavenumber-frequency model is given by [10]

$$\tilde{\phi}_{pp}(k_x, k_y, \omega) = \frac{2\pi \left(\alpha_x \alpha_y\right)^2 k_c^3}{\left(\alpha_x \alpha_y k_c\right)^2 + \left(\alpha_x k_y\right)^2 + \left(\alpha_y^2 \left(k_x - k_c\right)^2\right)^{3/2}} \tag{B.2}$$

where $\alpha_x = 0.1$ and $\alpha_y = 0.77$.

References

[1] E. Ciappi, S. De Rosa, F. Franco, J.-L. Guyader, S. A. Hambric, Flinovia: Flow Induced Noise and Vibration Issues and Aspects-I, Springer, 2015.

[2] E. Ciappi, S. De Rosa, F. Franco, J.-L. Guyader, S. A. Hambric, R. C. K. Leung, A. D. Hanford, Flinovia: Flow Induced Noise and Vibration Issues and Aspects-II, Springer, 2019.

[3] E. Ciappi, S. De Rosa, F. Franco, S. A. Hambric, R. C. Leung, V. Clair, L. Maxit, N. Totaro, Flinovia–Flow Induced Noise and Vibration Issues and Aspects-III, Springer, 2021.

[4] E. Ciappi, F. Magionesi, S. De Rosa, F. Franco, Hydrodynamic and hydroelastic analyses of a plate excited by the turbulent boundary layer, J. Fluids Struct. 25 (2009) 321–342. https://doi.org/10.1016/j.jfluidstructs.2008.04.006.

[5] S. A. Hambric, Y. F. Hwang, W. K. Bonness, Vibrations of plates with clamped and free edges excited by low-speed turbulent boundary layer flow, J. Fluids Struct. 19 (2004) 93–110. https://doi.org/10.1016/j.jfluidstructs.2003.09.002.

[6] W. K. Bonness, D. E. Capone, S. A. Hambric, Low-wavenumber turbulent boundary layer wall-pressure measurements from vibration data on a cylinder in pipe flow, J. Sound Vib. 329 (2010) 4166–4180. https://doi.org/10.1016/j.jsv.2010.04.010.

[7] K. M. Cipolla, W. L. Keith, Measurements of the wall pressure spectra on a full-scale experimental towed array, Ocean Eng. 35 (2008) 1052–1059. https://doi.org/10.1016/j.oceaneng.2008.02.006.

[8] N. Martin, P. Leehey, Low wavenumber wall pressure measurements using a rectangular membrane as a spatial filter, J. Sound Vib. 52 (1977) 95–120. https://doi.org/10.1016/0022-460X(77)90391-1.

[9] G. Corcos, The structure of the turbulent pressure field in boundary-layer flows, J. Fluid Mech. 18 (1964) 353–378. https://doi.org/10.1017/S002211206400026X.

[10] R. H. Mellen, On modeling convective turbulence, J. Acoust. Soc. Am. 88 (1990) 2891–2893. https://doi.org/10.1121/1.399695.

[11] D. M. Chase, Modeling the wavevector-frequency spectrum of turbulent boundary layer wall pressure, J. Sound Vib. 70 (1980) 29–67. https://doi.org/10.1016/0022-460X(80)90553-2.

[12] X. Zhao, M. Guo, J. Lei, Updating of wavenumber-frequency spectrum models by a phased array measurement, Aerosp. Sci. Technol. 107 (2020) 106273. https://doi.org/10.1016/j.ast.2020.106273.

[13] S. Haxter, C. Spehr, Wavenumber characterization of surface pressure fluctuations on the fuselage during cruise flight, in: Flinovia—Flow Induced Noise and Vibration Issues and Aspects-III, Springer, 2021, pp. 157–180. https://doi.org/10.1007/978-3-030-64807-7_8.

[14] R. Merino-Martínez, P. Sijtsma, M. Snellen, T. Ahlefeldt, J. Antoni, C. J. Bahr, D. Blacodon, D. Ernst, A. Finez, S. Funke, et al., A review of acoustic imaging methods using phased microphone arrays:

Part of the "aircraft noise generation and assessment" special issue, CEAS Aeronaut. J. 10 (2019) 197–230. https://doi.org/10.1007/s13272-019-00383-4.

[15] E. Sarradj, Three-dimensional acoustic source mapping with different beamforming steering vector formulations, Adv. Acoust. Vib. 2012 (2012). https://doi:10.1155/2012/292695.

[16] M. Karimi, L. Maxit, Acoustic source localisation using vibroacoustic beamforming, Mech. Syst. Signal Process. 199 (2023) 110454. https://doi.org/10.1016/j.ymssp.2023.110454.

[17] Q. Leclere, A. Dinsenmeyer, E. Salze, J. Antoni, A comparison between different wall pressure measurement devices for the separation and analysis of tbl and acoustic contributions, in: Flinovia—Flow Induced Noise and Vibration Issues and Aspects-III, Springer, 2021, pp. 181–206. https://doi.org/10.1007/978-3-030-64807-7_9.

[18] R. L. Panton, G. Robert, The wavenumber-phase velocity representation for the turbulent wall-pressure spectrum, J. Fluids Eng. 116 (1994) 477–483. https://doi.org/10.1115/1.2910301.

[19] G. Maidanik, Flush-mounted pressure transducer systems as spatial and spectral filters, J. Acoust. Soc. Am. 42 (1967) 1017–1024. https://doi.org/10.1121/1.1910683.

[20] W. K. Blake, D. M. Chase, Wavenumber-frequency spectra of turbulent-boundary-layer pressure measured by microphone arrays, J. Acoust. Soc. Am. 49 (1971) 862–877. https://doi.org/10.1121/1.1912427.

[21] F. Geib, T. Farabee, Measurement of boundary layer pressure fluctuations at low wavenumber on smooth wall, J. Acoust. Soc. Am. 59 (1976) S45–S45. https://doi.org/10.1121/1.2002710.

[22] S. Damani, H. Butt, J. T. Banks, S. Srivastava, N. A. Balantrapu, T. Lowe, W. J. Devenport, Low-wavenumber wall pressure measurements in zero-pressure gradient boundary layer flow, in: AIAA SCITECH 2022 Forum, 2022, p. 1795. https://doi.org/10.2514/6.2022-1795.

[23] N. Hu, Sensor-size-related attenuation correction of wall pressure spectra measurements, Phys. Fluids. 34 (2022). https://doi.org/10.1063/5.0094847.

[24] G. Corcos, The resolution of turbulent pressures at the wall of a boundary layer, J. Sound Vib. 6 (1967) 59–70. https://doi.org/10.1016/0022-460X(67)90158-7.

[25] E. Manoha, The wavenumber-frequency spectrum of the wall pressure fluctuations beneath a turbulent boundary layer, in: Aeroacoustics Conference, 1996, p. 1758. https://doi.org/10.2514/6.1996-1758.

[26] P. Bremner, C. Todter, S. Clifton, Sideglass turbulence and wind noise sources measured with a high resolution surface pressure array, SAE Int. J. Passeng. Cars - Mech. 8 (2015). https://doi.org/10.4271/2015-01-2325.

[27] É. Salze, C. Bailly, O. Marsden, E. Jondeau, D. Juvé, An experimental characterisation of wall pressure wavevector-frequency spectra in the presence of pressure gradients, in: 20th AIAA/CEAS Aeroacoustics Conference, 2014, p. 2909. https://doi.org/10.2514/6.2014-2909.

[28] B. Arguillat, D. Ricot, C. Bailly, G. Robert, Measured wavenumber: Frequency spectrum associated with acoustic and aerodynamic wall pressure fluctuations, J. Acoust. Soc. Am. 128 (2010) 1647–1655. https://doi.org/10.1121/1.3478780.

[29] B. Arguillat, D. Ricot, G. Robert, C. Bailly, Measurements of the wavenumber-frequency spectrum of wall pressure fluctuations under turbulent flows, in: 11th AIAA/CEAS aeroacoustics conference, 2005, p. 2855. https://doi.org/10.2514/6.2005-2855.

[30] S. Haxter, C. Spehr, Infinite beamforming: wavenumber decomposition of surface pressure fluctuations, in: Proceedings of the 5th Berlin Beamforming Conference, 2014, pp. 1–10. https://api.semanticscholar.org/CorpusID:93342136.

[31] R. Dougherty, Extensions of damas and benefits and limitations of deconvolution in beamforming, in: 11th AIAA/CEAS aeroacoustics conference, 2005, p. 2961. https://doi.org/10.2514/6.2005-2961.

[32] J. R. Underbrink, Aeroacoustic phased array testing in low speed wind tunnels, in: Aeroacoustic measurements, Springer, 2002, pp. 98–217. https://doi.org/10.1007/978-3-662-05058-3_3.

[33] C. F. Schram, N. Van de Wyer, An optimized microphone array for the measurement of turbulent boundary layer wall pressure wavenumber-frequency spectra, in: 2018 AIAA/CEAS Aeroacoustics Conference, 2018, p. 2968. https://doi.org/10.2514/6.2018-2968.

[34] K. Ehrenfried, L. Koop, Pressure fluctuations beneath a compressible turbulent boundary layer, in: 14th AIAA/CEAS Aeroacoustics Conference (29th AIAA Aeroacoustics Conference), 2008, p. 2800. https://doi.org/10.2514/6.2008-2800.

[35] S. Haxter, J. Brouwer, J. Sesterhenn, C. Spehr, Obtaining phase velocity of turbulent boundary layer pressure fluctuations at high subsonic Mach number from wind tunnel data affected by strong background noise, J. Sound Vib. 402 (2017) 85–103. https://doi.org/10.1016/j.jsv.2017.05.011.

[36] S. L. Prigent, É. Salze, C. Bailly, Deconvolution of wave-number-frequency spectra of wall pressure fluctuations, AIAA J. 58 (2020) 164–173. https://doi.org/10.2514/1.J058203.

[37] L. Maxit, Simulation of the pressure field beneath a turbulent boundary layer using realizations of uncorrelated wall plane waves, J. Acoust. Soc. Am. 140 (2016) 1268–1285. https://doi.org/10.1121/1.4960516.

[38] P. C. Hansen, Regularization tools version 4.0 for Matlab 7.3, Numerical algorithms 46 (2007) 189–194. https://doi.org/10.1007/s11075-007-9136-9.

[39] R. Campagna, L. D'Amore, A. Murli, An efficient algorithm for regularization of Laplace transform inversion in real case, J. Comput. Appl. Math. 210 (2007) 84–98. https://doi.org/10.1016/j.cam.2006.10.077.

[40] M. Bertero, P. Brianzi, E. R. Pike, L. Rebolia, Linear regularizing algorithms for positive solutions of linear inverse problems, Proc. Math. Phys. Eng. Sci. 415 (1988) 257–275. https://doi.org/10.1098/rspa.1988.0013.

[41] G. Rodriguez, D. Theis, An algorithm for estimating the optimal regularization parameter by the L-curve, Rendiconti di Mat. e delle Sue Appl. 25 (2005) 69–84. https://api.semanticscholar.org/CorpusID:124151821.

[42] P. C. Hansen, T. K. Jensen, G. Rodriguez, An adaptive pruning algorithm for the discrete L-curve criterion, J. Comput. Appl. Math. 198 (2007) 483–492. https://doi.org/10.1016/j.cam.2005.09.026.

[43] W. Graham, Boundary layer induced noise in aircraft, Part I: The flat plate model, J. Sound Vib. 192 (1996) 101–120. https://doi.org/10.1006/jsvi.1996.0178.

[44] W. Graham, A comparison of models for the wavenumber–frequency spectrum of turbulent boundary layer pressures, J. Sound Vib. 206 (1997) 541–565. https://doi.org/10.1006/jsvi.1997.1114.

[45] T. S. Miller, J. M. Gallman, M. J. Moeller, Review of turbulent boundary layer models for acoustic analysis, J. Aircr. 49 (2012) 1739–1754. https://doi.org/10.2514/1.C031405.

[46] M. Karimi, P. Croaker, L. Maxit, O. Robin, A. Skvortsov, S. Marburg, N. Kessissoglou, A hybrid numerical approach to predict the vibrational responses of panels excited by a turbulent boundary layer, J. Fluids Struct. 92 (2020) 102814. https://doi.org/10.1016/j.jfluidstructs.2019.102814.

[47] M. Bull, Wall-pressure fluctuations associated with subsonic turbulent boundary layer flow, J. Fluid Mech. 28 (1967) 719–754. https://doi.org/10.1017/S0022112067002411.

[48] A. V. Oppenheim, R. W. Schafer, J. R. Buck, Discrete-Time Signal Processing, second ed., Prentice-hall Englewood Cliffs, 1999.

[49] M. Goody, Empirical spectral model of surface pressure fluctuations, AIAA J. 42 (2004) 1788–1794. https://doi.org/10.2514/1.9433.

[50] R. A. Haubrich, Array design, Bull. Seismol. Soc. Am. 58 (1968) 977–991. https://doi.org/10.1785/BSSA0580030977.

[51] M. Karimi, P. Croaker, A. Skvortsov, D. Moreau, N. Kessissoglou, Numerical prediction of turbulent boundary layer noise from a sharp-edged flat plate, Int. J. Numer. 90 (2019) 522–543. https://doi.org/10.1002/fld.4733.